January 01, 2008

Hemodynamically constrained dynamic diffuse optical tomography under mammographic compression: simulation study

Eleonora Vidolova
Northeastern University

NORTHEASTERN UNIVERSITY

Graduate School of Engineering

Thesis Title: Hemodynamically Constrained Dynamic Diffuse Optical Tomography Under Mammographic Compression: Simulation Study

Author: Eleonora Vidolova

Department: Electrical and Computer Engineering

Approved for Thesis Requirement of the Master of Science Degree

Dana Brooks, Thesis Adviser	Date
Eric Miller, Thesis Reader	Date
David Boas, Thesis Reader	Date
Stefan Carp, Thesis Reader	Date
, Department Chair	Date

Gradate School Notified of Acceptance:

Director of the Graduate School	Date

HEMODYNAMICALLY CONSTRAINED DYNAMIC DIFFUSE OPTICAL TOMOGRAPHY UNDER MAMMOGRAPHIC COMPRESSION: SIMULATION STUDY

A Thesis Presented

by

Eleonora Vidolova

to

The Department of Electrical and Computer Engineering

in partial fulfillment of the requirements for the degree of

Master of Science
in

Electrical Engineering

in the field of

Communications and Signal Processing

Norhteastern University

Boston, Massachusetts

June 2008

ABSTRACT

HEMODYNAMICALLY CONSTRAINED DYNAMIC DIFFUSE OPTICAL TOMOGRAPHY UNDER MAMMOGRAPHIC COMPRESSION: SIMULATION STUDY

Eleonora Vidolova

Department of Electrical and Computer Engineering

Master of Science

Diffuse optical tomography (DOT) is an imaging modality with potential use in breast cancer detection, diagnosis and monitoring, brain imaging, and small animal imaging. In this work we focus on breast cancer imaging. It has been observed that malignant and normal tissues differ in blood flow (F) and oxygen consumption (OC). We are interested in using DOT to image those parameters since they are functionallly related to the main absorbers of near infrared light in tissue, oxygenated and deoxygenated hemoglobin. In particular we look at dynamic changes in F and OC when the breast is put under mammographic compression, as is done using an experimental combined X-ray/DOT system under development by our collaborators at Mass General Hospital. It is believed that these changes provide a potential source of contrast between tumor and other tissue. In this work we analyze, in a simulation scenario, the ability of the imposition of a hemodynamically constrained model of temporal

changes in oxygen saturation (SO_2) to improve our algorithm for extracting OC and F from reconstruction of hemoglobin concentrations. Using a three dimensional transmission measurement geometry we investigate how the recovery of metabolic parameters is influenced by the observation time interval, the SNR of the measurements, the regularization parameter choices, and a assumptions about the dynamic behavior of total hemoglobin concentration. We conclude that we can reconstruct a 1.5x OC and 2.5x F contrast for a spherical inclusion with less than 20% error as long as we use at least 90 seconds of 60dB SNR data even in the presence of variations in total hemoglobin concentration. Further more we have noticed that by introducing a dynamic model we are able to somewhat compensate for the errors in the reconstructed tumor OC.

ACKNOWLEDGMENTS

I would like to acknowledge Prof. Dana Brooks for all the support, useful advice, and understanding. I would also want to thank Prof. Eric Miller, Stefan Carp, and Dr. David Boas for the help on my research project. I would also want to mention all my colleagues from the Biomedical Image and Signal Processing Group, all of them helped me a lot during my time in Northeastern. Last but not least I would like to thank my family and friends for believing in me and always being there for me.

Contents

List of Figures

Chapter 1

Introduction

1.1 Diffuse Optical Tomography - Overview

Diffuse optical tomography (DOT) is an imaging modality with potential use in breast cancer detection, diagnosis and monitoring [1,3,6,8,16,17,26,28], brain imaging [18], and small animal imaging [15]. DOT uses near infrared light (NIR) to illuminate biological tissue. Light that transmits through the tissue is detected and a propagation model is used to determine the properties of the imaged tissue. The main absorbers of NIR light in tissue are oxygenated and deoxygenated hemoglobin, and since they have different spectral signatures [7], Figure 1.1, we can use light at two or more different wavelengths to reconstruct their concentrations.

Reasons why researchers have been interested in DOT include relatively low cost and the good time resolution. Another motivation to use DOT is that NIR light is not harmful and yet can penetrate several centimeters through tissue. DOT can also complement structural imaging modalities, such as X-ray, ultrasound, or MRI, by providing functional information about tissue hemoglobin species concentration, which is related to tissue vascularization and metabolism.

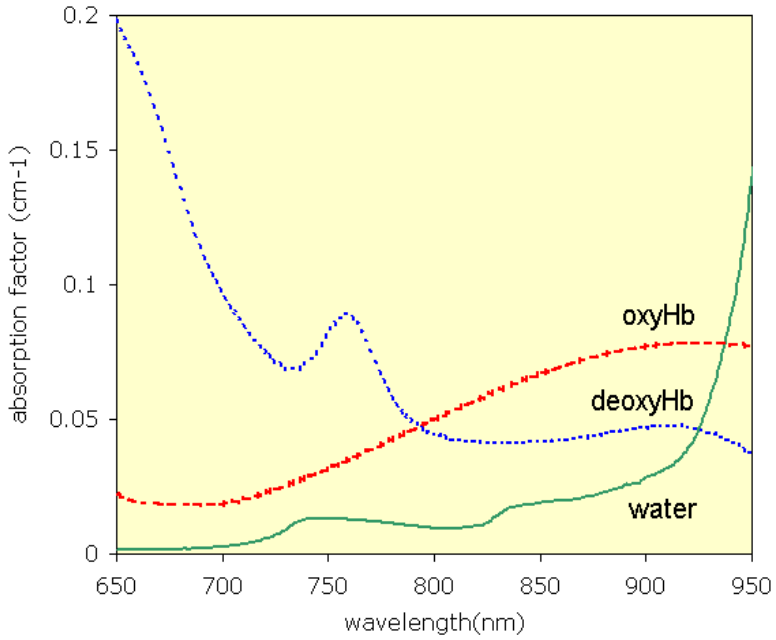

Figure 1.1 HbO and HbR spectra [4]

1.2 DOT for Breast Imaging

In this thesis we focus on DOT for breast cancer imaging. Breast cancer tumors are known to have increased vascularization [14] and information on tumor angiogenesis can help determine malignancy [27]. Furthermore, oxygen consumption (OC) and blood flow (F) contrasts between malignant and normal tissue have been observed by Beaney [2, 29] and Durduran [12]. Thus, hemoglobin concentration, blood flow and oxygen consumption could help specify the degree of malignancy of a tumor. DOT can be used to image these functional parameters because the main light absorbers in tissue are oxygenated and deoxygenated hemoglobin. This information may be further combined with structural information from any anatomical imaging method to improve breast cancer screening [30].

The work on this thesis was carried out in collaboration with Stefan Carp and David Boas from the Photon Migration Imaging (PMI) laboratory at the Athinoula A. Martinos Center for Biomedical Imaging. Their group is investing the use of DOT for breast cancer imaging in conjunction with X-ray mammographic measurements. Thus, in this work we are looking into models that describe the hemodynamic changes due to mammographic compression. A detailed description of our setup is given in section 2.6. One advantage of this approach, that might help improve OC and F reconstructions, is that we can get additional functional information due to the hemodynamic changes induced by the compression. Other researchers have investigated different imaging strategies, for example where the patient's breast is suspended in a cylindrical cavity and the optics are mounted around the circumference of the cavity [22, 26]. Related research in breast cancer detection using NIR light using manually scannable detectors has also been done by some groups [23].

1.3 Related Previous Work

Researchers from PMI laboratory at the Athinoula A. Martinos Center for Biomedical Imaging have been working on developing a multimodality imaging method combining X-ray mammography and DOT. Work has been done on coregistering the X-ray and optical data [30]. Further more as part of this work a spectroscopy study was performed to characterize the influence of mammographic like compression on the physiology of the breast [5, 24].

Since F and OC are important biological parameters that give information about a tumor's metabolic activity researchers have been interested in measuring them. In his study of the compression induced hemodynamic changes in the breast, Carp et al. [5] has also looked at F and OC reconstructions. Durduran et al. [12] has also worked on measuring F using DOT, in their study the measurements were taken using a handheld probe. There have also been studies using positron emission tomography (PET) to study those parameters. For example a clinical study has been done by Wilson et al. [29] to measure blood flow in breast tumors, and Beaney et al. [2] used PET to measure both blood flow and oxygen utilization in patients with breast carcinoma.

1.4 Contribution of this Thesis

This study is motivated by results obtained by the Photon Migration Lab at MGH from a combined X-ray and optical imaging device [30], where it was observed that if DOT measurements were taken in a mammography setting the compression-induced changes in the breast hemodynamics may be significant, and indeed possibly a useful source of additional contrast, and should be taken into account during the optical image reconstruction [5]. In this thesis we evaluate the limitations of the new hemo-

dynamic model we developed. We explore whether improving the model improves reconstructions of OC and F. In this work we employ a hemodynamic model which takes into account compression-induced changes in the breast. Improving on the model described in [5], this model incorporates time variation of the tissue hemoglobin as seen in collected data. Using this model we conducted a feasibility study, through simulations, to test our ability to reconstruct OC and F. We report on the influence on the reconstruction process of the tissue total hemoglobin concentration rate of change, the measurement time intervals over which the data are acquired, the regularization parameter, and the sampling rate. We also estimate the additional error in OC and F reconstructions due to assuming $[HbT]_t$ is constant in cases where this is not true.

This thesis is structured in the following way: Chapter 2 gives details on our OC and F imaging strategy. In particular we describe the hemodynamic model we derived and how we validated that derivation, the forward model and HbO and HbR inverse solution we employed and our method for estimation of HbT and OC and F. We also describe the simulation setup, which includes the geometries and parameter values used. In Chapter 3 we show the results and observations from our study, and Chapter 4 presents our conclusions. In the Appendix we have included the detailed derivation of the hemodynamic model.

Chapter 2

OC and F Imaging Strategy

In this chapter we describe in detail the OC and F imaging strategy we used in this study. Figure 2.1 shows the steps we have taken in the simulations. We first assigned values for physiological parameters within a simulation volume containing a homogeneous background and a spherical inhomogeneity, computed the time evolution of $[HbT]_t(t)$ and $SO_2(t)$ (he hemodynamic model we used for those is described in section 2.1) and finally predicted the resulting time-resolved optical properties. The different geometries we used and the parameter values assigned for these simulations are given in section 2.6. Next we generated simulated optical measurements with added noise. From the simulated measurements we solved an inverse problem, using Tikhonov regularization, at each time instant, to directly estimate the concentrations of oxy- and deoxy-hemoglobin [21]. From these estimated concentrations we computed estimates of the oxygen saturation, $SO_2(t)$, and the total tissue hemoglobin, $[HbT]_t(t)$, and then further approximated the temporal evolution of the later estimates by fitting a straight line to them. Finally using the $SO_2(t)$ reconstructions and the estimated slope and intersect for each voxel, we perform a nonlinear least squares fit, described in section 2.5, to a first order ODE for $SO_2(t)$, parameterized by OC

and F, to recover the spatial distribution of OC and F.

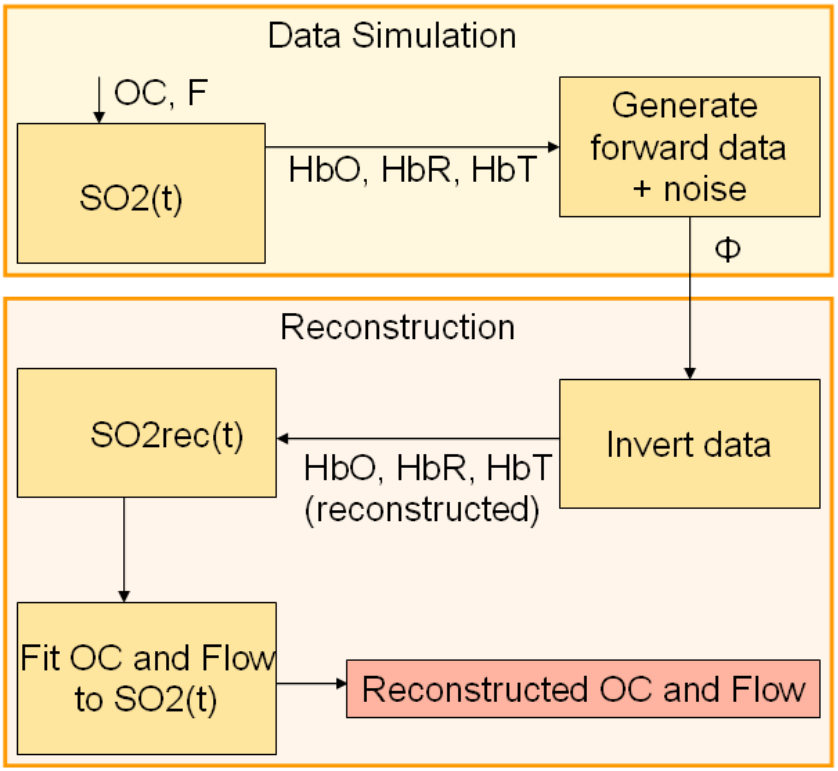

Figure 2.1 Flow chart of the steps taken in the simulations in this study

2.1 Hemodynamic Model

We use the hemodynamic model developed by Carp et al. [5] to predict the time course of hemodynamic changes due to tissue compression. To derive a solution for $SO_2(t)$ we began with the mass balance equation described in [5]:

$$\frac{d[HbO_2]}{dt} = -\frac{OC}{4V_t} + \frac{F_{in}[HbT]_b S_{a,O_2}}{V_t} - \frac{F_{out}[HbT]_b S_{v,O_2}}{V_t} \tag{2.1}$$

where $[HbO_2]$ is the time-varying molar concentration of oxygenated hemoglobin in tissue, OC is the tissue oxygen consumption (mol O_2.s^{-1}), F_{in} and F_{out} are the volume of blood flow into and out of the measurement volume respectively (Ls^{-1}), $[HbT]_b$ is the blood total hemoglobin concentration, S_{a,O_2} and S_{v,O_2} are the arterial and venous oxygen saturation, and V_t is the measurement volume.

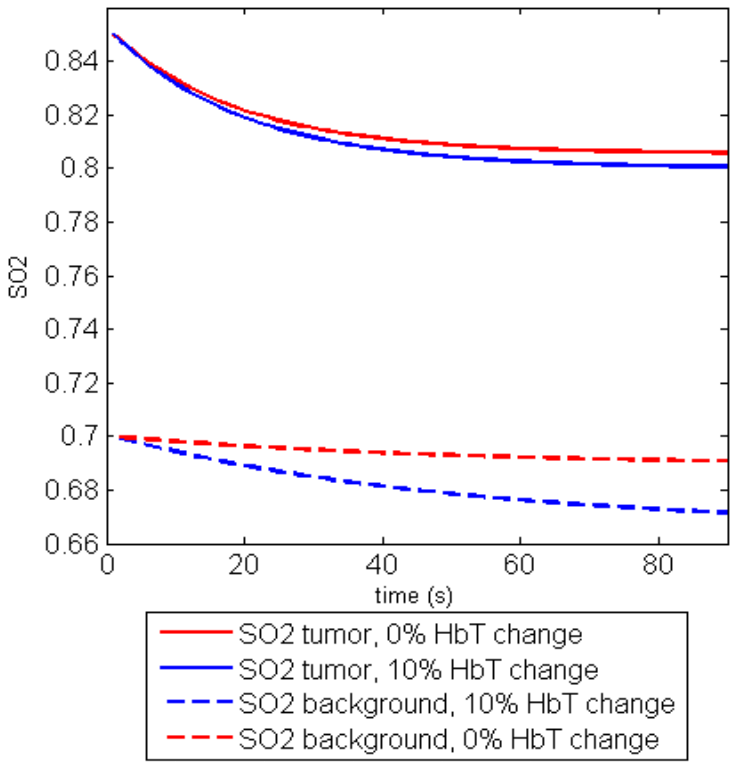

Figure 2.2 Simulated SO_2(t) time curves for tumor and background regions for both constant and linearly changing $[HbT]_t$

Assumptions made in the derivation in Ref. [5] were that blood inflow equaled blood outflow and that the total hemoglobin concentration in the entire tissue volume $[HbT]_t$ (tissue total hemoglobin concentartion) was constant. Volunteer data, not yet published, acquired in the PMI laboratory at MGH has shown that those assumptions are correct in some cases but that in others there were dynamic changes in the

total hemoglobin concentration when the patient's breast was under mammographic compression. Thus in the current simulations we have incorporated a time-varying $[HbT]_t$. Many subjects exhibited an almost linear increase in $[HbT]_t$, hence in this feasibility study we assumed such a linear change:

$$[HbT]_t(t) \approx a + bt. \tag{2.2}$$

Thus the relationship between blood inflow and outflow becomes:

$$\frac{F_{out}}{V_t} = \frac{F_{in}}{V_t} - \frac{d[HbT]_t}{dt}\frac{1}{[HbT]_b} = \frac{F_{in}}{V_t} - \frac{b}{[HbT]_b}. \tag{2.3}$$

We also assumed that $SO_2(t)$ is a weighted average of the arterial and venous saturations [**?**]:

$$SO_2(t) = fS_{a,O_2} + (1-f)S_{v,O_2} \tag{2.4}$$

Where here we take the weight factor $f = \frac{1}{2}$. Since $[HbO_2] = SO_2[HbT]_t$:

$$\frac{d[HbO_2]}{dt} = SO_2(t)\frac{d[HbT]_t}{dt} + \frac{dSO_2}{dt}[HbT]_t(t) \tag{2.5}$$

By combining equations (2.1) through (2.5) we get the ordinary differential equation below with initial condition $SO_2(t=0) = SO_{2,init}$.

$$\frac{dSO_2(t)}{dt} = \frac{1}{a+bt}\Bigg(- bSO_2(t) - \frac{OC}{4V_t} + \frac{F_{in}}{V_t}[HbT]_{bl}SaO_2 - \left(\frac{F_{in}}{V_t} - \frac{b}{[HbT]_{bl}}\right)[HbT]_{bl}\left(2SO_2(t) - SaO_2\right)\Bigg) \tag{2.6}$$

After some recombining of variables we can manipulate Eq. 2.6 into the following form:

$$\frac{dSO_2}{dt} = \frac{SO_2C + D}{a + bt}, \tag{2.7}$$

where $C = b - 2\frac{F_{in}}{V}[HbT]_{bl}$ and $D = -SaO_2\left(b - 2\frac{F_{in}}{V}[HbT]_{bl}\right) - \frac{OC}{4V}$ (all the parameters in C and D are constant. Solving Eq. 2.7 (the details of the solution are given in Appendix A), plugging C and D back in, and rearranging we get:

$$SO_2(t) = SO_{2,init}\left(\frac{a+bt}{a}\right)^{1-2\frac{F_{in}}{V_t}\frac{[HbT]_{bl}}{b}} + \left(SaO_2 + \frac{OC}{4V_t\left(b - 2\frac{F_{in}}{V_t}[HbT]_{bl}\right)}\right)\left(1 - \left(\frac{a+bt}{a}\right)^{1-2\frac{F_{in}}{V_t}\frac{[HbT]_{bl}}{b}}\right) \tag{2.8}$$

The $SO_2(t)$ equation derived here was used to simulate $[HbO_2]$ and $[HbR]$ concentrations for each voxel in the given volume. Figure 2.2 shows sample time curves for the oxygen saturation generated using equation 2.8 for background and tumor regions and 0%[1] and 10% change in $[HbT]_t$. To generate the data in Figure 2.2 we used physiologically realistic parameters as described in section 2.6. For a all the steps taken in derivation of the hemodynamic model you can refer to Appendix A.

2.1.1 Model Verification

In order to verify this analytical solution of the ODE, we also solved it numerically using MATLAB's *ode45*. We used the same parameter values in both the analytical solution and in the numerical solution. As shown in Figure 2.3 the two solutions match. Figure 2.3 also verifies that our analytical solution reverts to the previous analytical solution when we assume $[HbT]_t$ constant.

[1]Due to the division by b in equation 2.8 we used $b = 10^{-15}$ μM/L to avoid dividing by 0. If exactly $b = 0$ needs to be used, the solution of ODE can be obtained numerically using the desired parameters ($b = 0$) at the expense of computational speed.

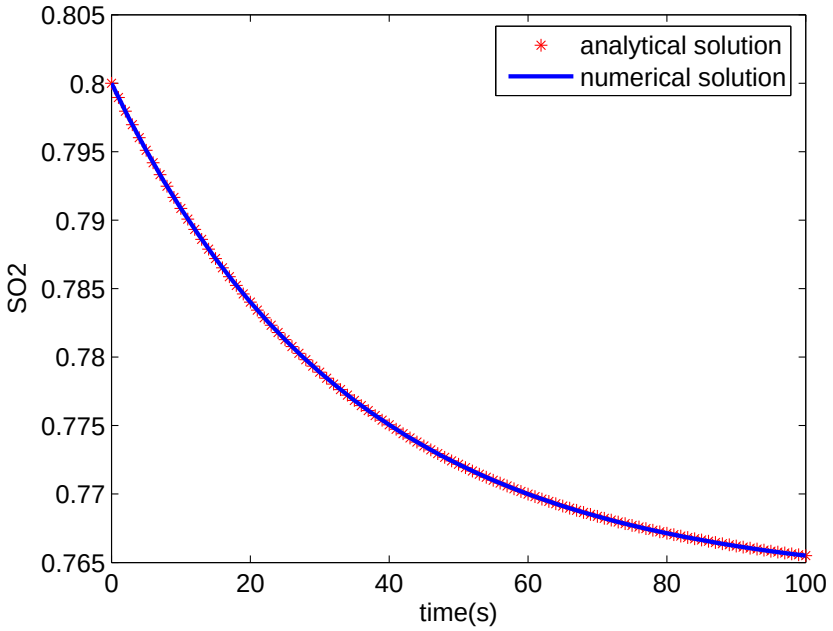

Figure 2.3 SO_2 time curves for the analytical and numerical solution

2.2 Forward Model

In order to compute the simulated fluence at the detectors (the geometries are described in section 2.6) and to map the fluence values back to the spatial absorption function, we need a model of light propagation in a highly scattering medium. The forward model we used is the Helmholtz frequency domain diffusion equation [13, 25]:

$$\left(\nabla^2 + k^2\right)\Phi(\mathbf{r},\mathbf{t}) = -\frac{\nu}{D}S(\mathbf{r},\mathbf{t}) \tag{2.9}$$

where $k^2 = \frac{-\nu\mu_a + j\omega}{D}$ is the complex wavenumber, $D = \frac{\nu}{3\mu_s'}$ is the diffusion coefficient, μ_s' is the reduced scattering coefficient, $\mu_s' = (1-g)\mu_s$, where μ_s is the optical scattering coefficient and g is the mean cosine of the phase function, $\Phi(\mathbf{r},t)$ is the photon fluence at position $\mathbf{r}$ at time t, μ_a is the absorption coefficient, ν is the electromagnetic propagation velocity in the medium, ω is the frequency and $S(\mathbf{r},t)$ is the

source function. The optical properties of the tissue, which are wavelength dependent, are directly related to physiological parameters. The absorption μ_a is dominated by hemoglobin, so we can express it in terms of the wavelength dependent extinction coefficients of HbO_2 and HbR and the hemoglobin concentrations, $[HbO_2]$ and $[HbR]$ [20, 21]. This way, if we have measurements at two or more different wavelengths we can solve for $[HbO_2]$ and $[HbR]$. We can write Φ for two wavelengths in terms of $[HbO_2]$ and $[HbR]$ as described by Li et al. [20, 21]. We used a perturbation approach, where the absorption coefficient and wavenumber were represented as homogeneous background values plus spatial perturbations. Using a Green's function approach we approximated the scattered field, and then used the first Born approximation to linearize the resulting PDE. A more detailed explanation of this forward model is given in [13, 25].

2.3 HbO and HbR Inverse Solution

In order to estimate the hemoglobin chromophore concentration given the linearized model, we have to solve the inverse problem. We do that independently at each time instant.

$$Ax = y + n \tag{2.10}$$

where x is a spatial vector of chromophores, y is the vector of measurements at two (or more) wavelengths, n is additive noise and $A \in R^{MXN}$ spatially maps $x \in R^{NX1}$ to $y \in R^{MX1}$. The forward matrix has a block form. The outermost block is the type of perturbation (if both are used); absorption first, then scattering. Within that block, the next set of blocks are by wavelength (so that the matrix correctly represents perturbations at multiple wavelengths). Finally, within each wavelength

is a dense matrix mapping perturbations at that wavelength into the scattered field. Since DOT is an ill-posed problem, we solve a regularized least-squares problem:

$$\min \|Ax - y\|_2^2 + \lambda R(x) \tag{2.11}$$

where $R(x)$ is the regularization term and λ the regularization parameter. In this study we used spectral information to directly reconstruct $[HbO_2]$ and $[HbR]$ at each time instant, using the method described by Li in [20, 21].

2.4 HbT Estimation

After we reconstructed the $[HbO_2]$ and $[HbR]$ time curves for each voxel we needed to estimate the a and b parameters of $[HbT]_t$ in equation 2.2. From $[HbT]_t = [HbO_2] + [HbR]$ we get the instentaneous value of $[HbT]_t$ for each voxel at each time point. Next we take the first time point to be a and we the value of t=60 sec to calculate b, using equation 2.2. Figure 2.4 shows the true $[HbT]_t$ time curve we used for the background values, the reconstructed $[HbT]_t$ time curve after solving the inverse problem for a sample voxel in the backgound, and the $[HbT]_t$ time curve we get using the estimated a and b values.

2.5 OC and F Estimation

After we have reconstructed the $[HbT]_t$, $[HbO_2]$ and $[HbR]$, values we obtain $SO_2(t)$ from the relationship $[HbO_2] = SO_2[HbT]_t$. Once we have the reconstructed $SO_2(t)$ over the time interval, we fit it to the hemodynamic model described in section 2.1 in order to get reconstructions for OC and F. We used two fitting techniques available in the MATLAB Optimization Toolbox - *lsqcurvefit* and *fminsearch*. Both methods

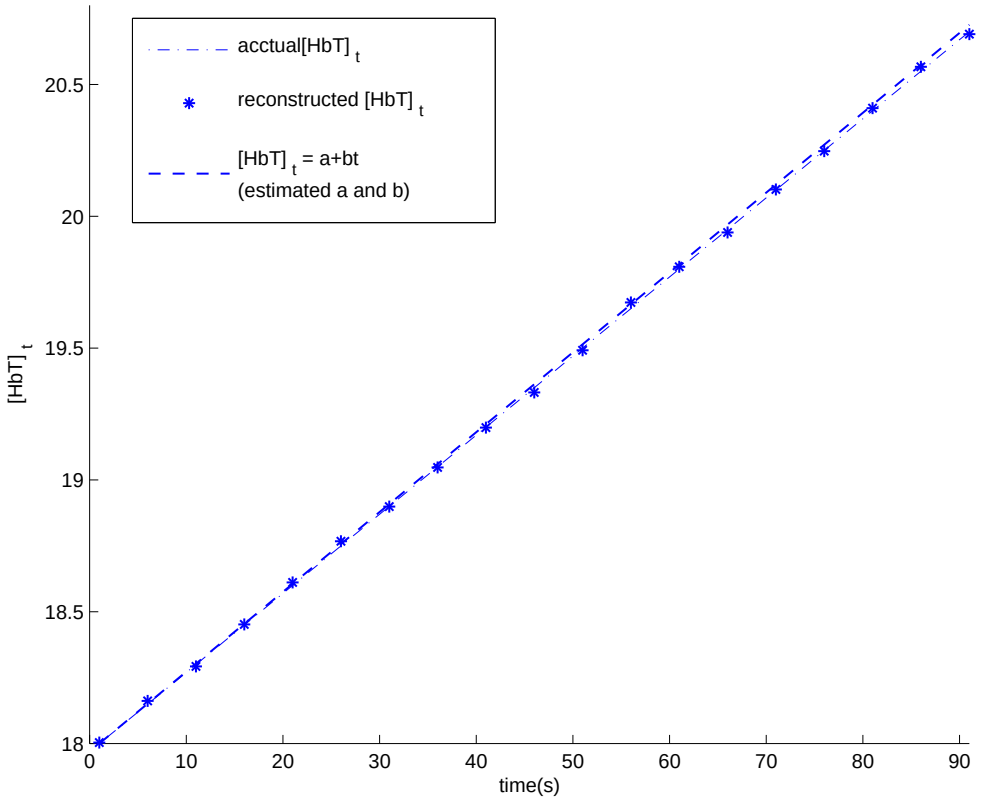

Figure 2.4 Actual $[HbT]_t$ time curve, reconstructed $[HbT]_t$ time curve, and $[HbT]_t = a + bt$ time curve based on estimated a and b

gave similar results. *lsqcurvefit* solves non-linear data-fitting problems in the least-squares sense. In our case, we found the coefficients $OC\ F$ that best fit equation 2.12 given the time t as input, and the observed output SO_2, rec, the reconstructed oxygen saturation, where t and SO_2, rec are vectors of length m and $\hat{SO_2}$ is a vector-valued function version of equation 2.8.

$$\min_{[OC\ F_{in}]} \frac{1}{2} \| \hat{SO_2}([OC\ F_{in}], t) - SO_2, rec(t) \|_2^2 \tag{2.12}$$

The algorithm used in *lsqcurvefit* is a subspace trust region method and is based on the interior-reflective Newton method described in [9] and [10]. Each iteration involves the approximate solution of a large linear system using the method of preconditioned conjugate gradients (PCG). The other method, *fminsearch*, finds the minimum of a problem specified by $\min_x f(x)$, where x is a vector and $f(x)$ is a function that returns a scalar. When using *fminsearch* we set up the least-squares problem described above in our own routine and fed its input to find the optimal solution using *fminsearch*. The algorithm used by *fminsearch* is the simplex search method described by Lagarias et al. [19].

2.6 Simulation Setup

In this section we describe the different geometries and parameter values we used in our study. We ran our simulations for three different slab geometries. The first one, described in Section 2.6.1, had a homogeneous background with one spherical tumor that had a sharp boundary between the background and tumor region. The second geometry, described in Section 2.6.2, also had a homogeneous background with one spherical inhomogeneity, but this time the contrast between tumor and background changed gradually. The last geometry we tested, described in Section 2.6.3, had a

homogeneous background, a bigger homogeneous spherical inclusion than in the first two geometries, and then a smaller sphere inside it. The goal in this last geometry is to represent the different breast types, fibroglandular and adipose tissues, and a tumor.

We added zero-mean Gaussian-distributed noise (i.e., representing electronic amplifier noise) to the simulated data before inversion. The Gaussian noise was sampled from a normal distribution, $\phi_{noise} = N(0, \sigma_{SNR})$, where, σ_{SNR} was selected such that the RMS signal to noise ratio was equal to the desired SNR.

2.6.1 One Sphere - Sharp Boundary

The first geometry used in our simulations was a uniform spherical inhomogeneity in a uniform background (Fig. 2.5). The imaged volume represents a slab of tissue with dimensions 10cm by 10cm by 6cm, which was treated computationally as infinite slab. There were 48 sources and 48 detectors, placed at $z = 0$ and $z = 6$ boundaries respectfully. One spherical inhomogeneity representing a tumor with diameter 3cm was placed at coordinates, 2cm, 2.25cm, 3.25cm.

For the first geometry (Fig. 2.5), when generating the data for our simulation we used the hemodynamic model described above in equation 2.8 to compute 90 seconds of data with a sample period of 5 seconds. We used $[HbT]_b = 700$ μM [5].The starting level for $[HbT]_t$ in tissue was $a = 18$ μM. We varied the rate of change in $[HbT]_t$ from 0%, to 5% and 10% over 60 seconds, i.e. $b = 0$ $\frac{\mu M}{s}$, $b = 0.015$ $\frac{\mu M}{s}$ and $b = 0.030$ $\frac{\mu M}{s}$. For the background blood flow we used $\frac{F_{b,in}}{V_t} = 0.000275$ (L/L/s) [5], and for the tumor blood flow we used $\frac{F_{t,in}}{V_t} = 2.5\frac{F_{b,in}}{V_t}$ (L/L/s). There have been a few studies on the contrast in blood flow between normal tissue and tumors, [2, 11, 29], which show the contrast to be around 5x. In our study we only use half of that value, 2.5x contrast, to represent a worst case scenario, given that our simulations are done

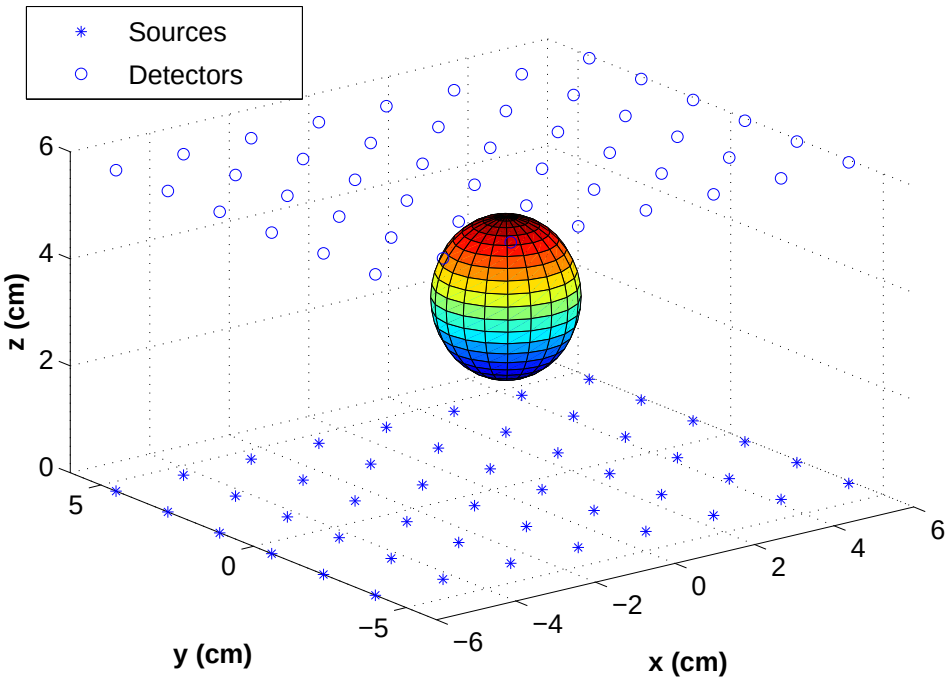

Figure 2.5 Geometry 1 - One sphere with sharp boundary

to represent geometry under compression. There have been no studies done so far on how compression affects the contrast in blood flow between normal and tumor tissue. In the study by Durduran et al. [12] the measurements were taken using a handheld probe, and the other OC and F studies were done using PET [2, 29]. For the background oxygen consumption we used $\frac{OC_b}{V_t} = 0.448$ μM/L/s, and for the tumor $\frac{OC_t}{V_t} = 1.5\frac{OC_b}{V_t}$ μM/L/s, since a PET study [2] has shown that the oxygen consumption in tumors is 1.5 times that of the normal tissue. We also assumed $S_{a,O_2} = 0.98$ from [5], $f = 0.5$ as stated before, $SO_{2,init,b} = 0.7$ for the background and $SO_{2,init,t} = 0.85$ for the tumor. The OC and F values are tabulated in Table 2.1.

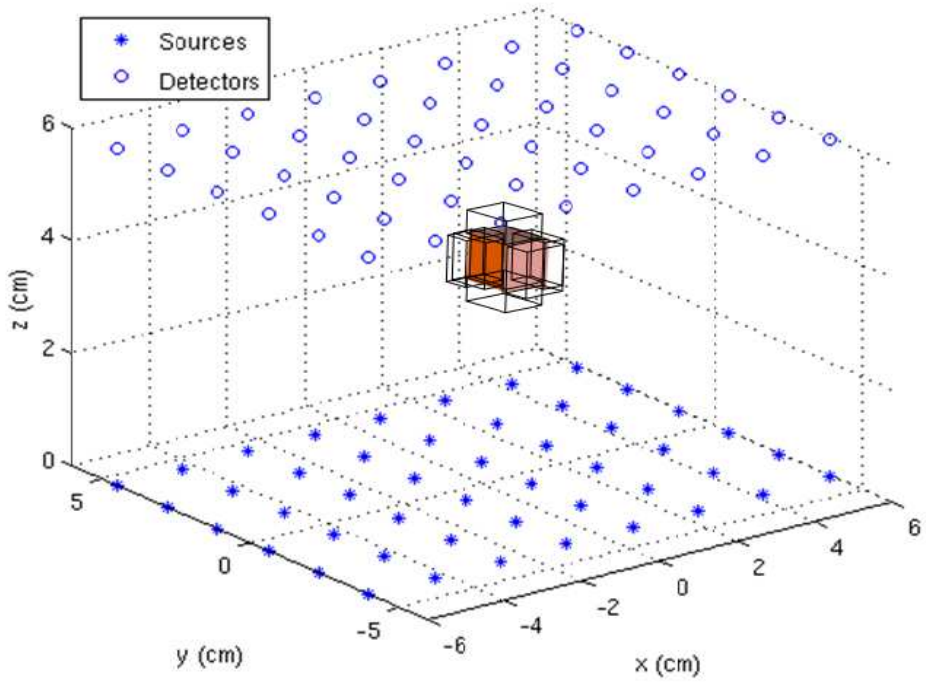

Figure 2.6 Geometry 2 - One sphere with gradual boundary

Table 2.1 OC and F parameter values for generated data for geometry 1

Parameter	Background	Tumor	Reference
F (L/L/s)	$2.75E{-}4$	$2.5 * 2.75E{-}4 = 6.785E{-}4$	[2, 5, 11, 29]
OC (μM/L/s)	0.448	$1.5 * 0.448 = 0.672$	[2]

2.6.2 One Sphere - Gradual Boundary

The second geometry we used had a uniform background and an inhomogeneity with a gradually changing contrast at the boundary. Again the volume used was 12cm by 12cm by 6cm slab. The tumor had two contrast levels for F relative to the background, one 2.5 times the background and the other 4 times the background, where the higher contrast value was in the center of the object (the red part of the object in Figure 2.6) and the lower on the outside. The higher contrast part of the inhomogeneity was a cube with 1cm sides, and the lower contrast parts were 0.5cm thick rectangles added on each side of the cube as shown in Figure 2.6. The object is located at coordinates 1.5cm, 1.5cm, 3cm. Other than the different contrast levels for F we kept all other parameter values the same as in the case with the sharp boundary sphere described in Section 3.1. A detailed description of the parameter values is given in Table 2.2 below.

Table 2.2 OC and F parameter values for generated data for geometry 2

Parameter	Background	Lower Contrast	Higher Contrast
F (L/L/s)	$2.75E{-}4$	$2.5 * 2.75E{-}4 = 6.785E{-}4$	$4 * 2.75E{-}4 = 11E{-}4$
OC (μM/L/s)	0.448	$1.5 * 0.448 = 0.672$	$1.5 * 0.448 = 0.672$

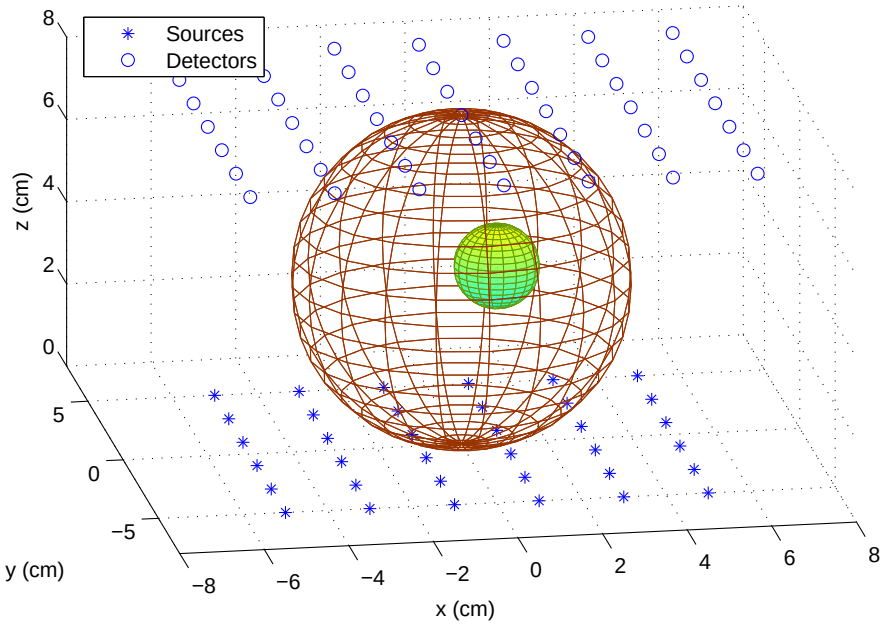

Figure 2.7 Geometry 3 - Sphere within a sphere

2.6.3 Sphere within a Sphere (SIS)

The third geometry was a uniform sphere within a larger sphere again in an uniform background (Fig. 2.7). This time the dimensions of the imaged volume were 12cm by 12cm by 8cm. There were 36 sources and 49 detectors, placed at $z = 0$cm and $z = 8$cm boundaries. One spherical inhomogeneity with radius 4cm was placed at coordinates 0cm, 0cm, 4cm. A smaller sphere with radius 1cm was placed within the bigger sphere, with center at coordinates 1cm, 1cm, 4cm. This geometry was intended as a more sophisticated caricature of the human female breast, with a tumor (the smaller sphere), embedded inside fibroglandular tissue, itself surrounded by adipose tissue. For this third geometry (Fig. 2.7) we changed the $SO_{2,init}$, OC and F values when generating the data in order to have contrast in the 3 different regions as specified in Table 2.3 below.

Table 2.3 OC and F parameter values for generated data for geometry 3

Parameter	Background	Big Sphere	Small Sphere
F (L/L/s)	$2.75E{-}4$	$2 * 2.75E{-}4 = 5.5E{-}4$	$3 * 2.75E{-}4 = 8.25E{-}4$
OC (μM/L/s)	0.448	$1.3 * 0.448 = 0.5824$	$1.6 * 0.448 = 0.7168$
$SO_{2,init}$	0.7	0.8	0.85

Chapter 3

Results and Observations

In this chapter we present the results of our study. In Sections 3.1, 3.2, 3.3 we show the results of the simulations using the three different geometries we used. In Section 3.4 we show the results of the error surfaces analysis we did.

3.1 One Sphere - Sharp Boundary

The results of our study for the sharp boundary geometry are summarized in Figures 3.1, 3.2, 3.3, 3.4. Figure 3.1 gives you an idea of what our results for geometry 1 look like, in this case the simulation was for 90s of data, 5% rate of change per minute for $[HbT]_t$, and SNR of 60dB. The top half of Figure 3.1 illustrates the OC and the bottom half the F reconstruction. Both halves display 12 slices through different depths in the z direction, starting from z=0.25cm at the top left and ending with z=5.75cm in the bottom right. Figure 3.2a shows that the relative error in the reconstructed OC and F depends on the rate of change in $[HbT]_t$. In particular the error was approximately constant with increasing rate of change for the background F and OC, increased for the tumor OC and decreased for the tumor F. The standard

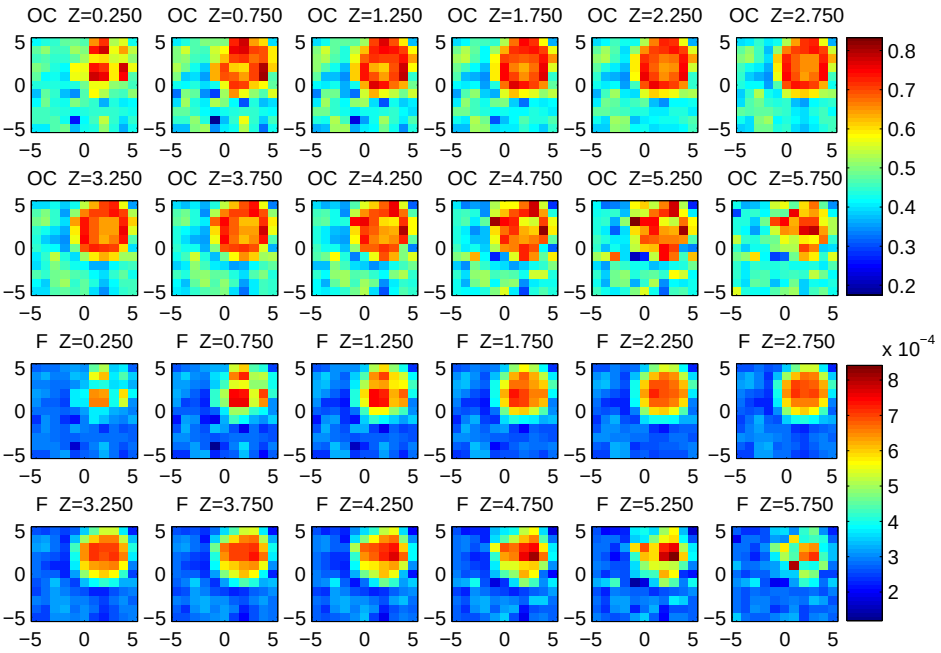

Figure 3.1 Results - One sphere, sharp boundary, 60dB SNR, 90s, 5% change in $[HbT]_t$ rate

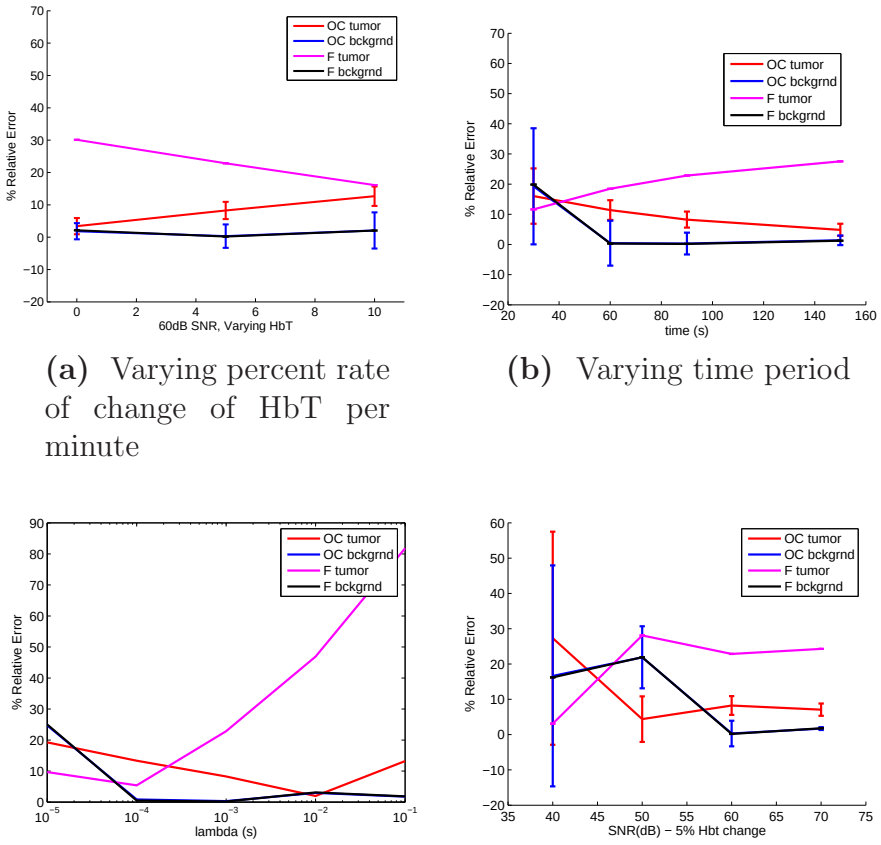

(a) Varying percent rate of change of HbT per minute

(b) Varying time period

(c) Varying regularization parameter

(d) Varying SNR

Figure 3.2 Influence of various choices for simulation and reconstruction parameters

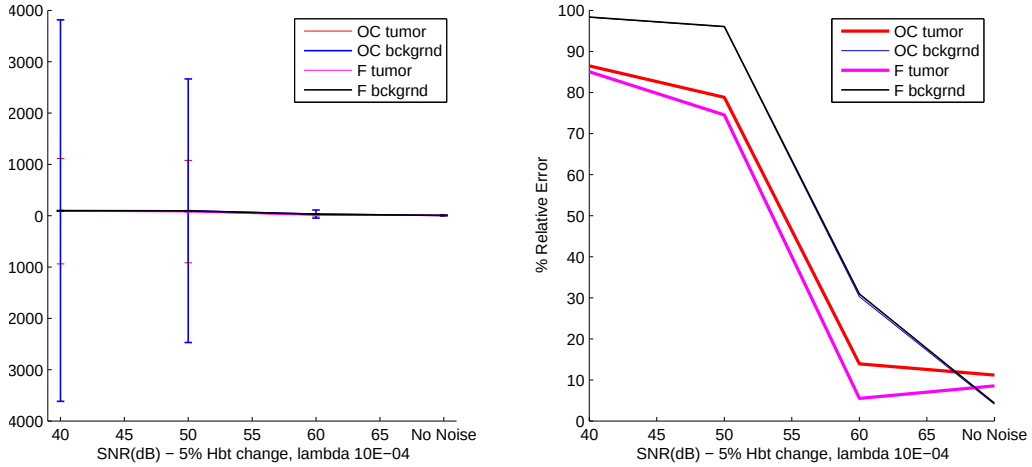

Figure 3.3 Relative error for varying SNR, regularization parameter 10^{-4}, HbT rate of change 5%

deviation of error in the tumor F was smaller than that of the background OC and F and the tumor OC. The influence of the length of the simulated measurement on the reconstructed parameters is shown on Figure 3.2b. As expected, in general if we used data for a longer time period we reconstruct parameters more accurately. We also varied SNR and as expected we got less relative error with higher SNR, Figure 3.2d. We speculate that the reason the relative error in the reconstructed tumor F did not decrease with higher SNR and grew, counter intuitively, when the time interval was increased due to the fact that the regularization parameter we used was not a good choice for the tumor F, as shown in Figure 3.2c. In order to confirm our hypothesis about tumor F in Figure 3.2 we ran our simulations with a regularization parameter of 10^{-4} for different SNR values, 90s of data, and 5% $[HbT]_t$ rate of change. The results of that simulation are shown in figure 3.3. Using the regularization parameter which is better for the tumor F we get less relative error in tumor F reconstructions, but the other hand the other parameters have bigger relative error and in addition to that we see much larger standard deviation. This result, together with the fact that our tumor SO_2 time curve reconstructions are lower than the true values, leads

us to believe that by introducing a dynamic model we are able to compensate for the errors in the reconstructed tumor OC but not the reconstructed tumor F. From the results in Figure 3.2 we conclude that we can reconstruct the F and OC parameters well (less than 20% error for tumor OC and background OC and F and less than 30% error for tumor F) for different rates of change in $[HbT]_t$, as long as we use at least 90 seconds of data, have a SNR of 60dB or higher, and use a regularization parameter of at least 10^{-3}. In addition to that, under those conditions we have enough visual contrast in our reconstructions to be able to distinguish between the tumor and the background regions, Figure 3.1.

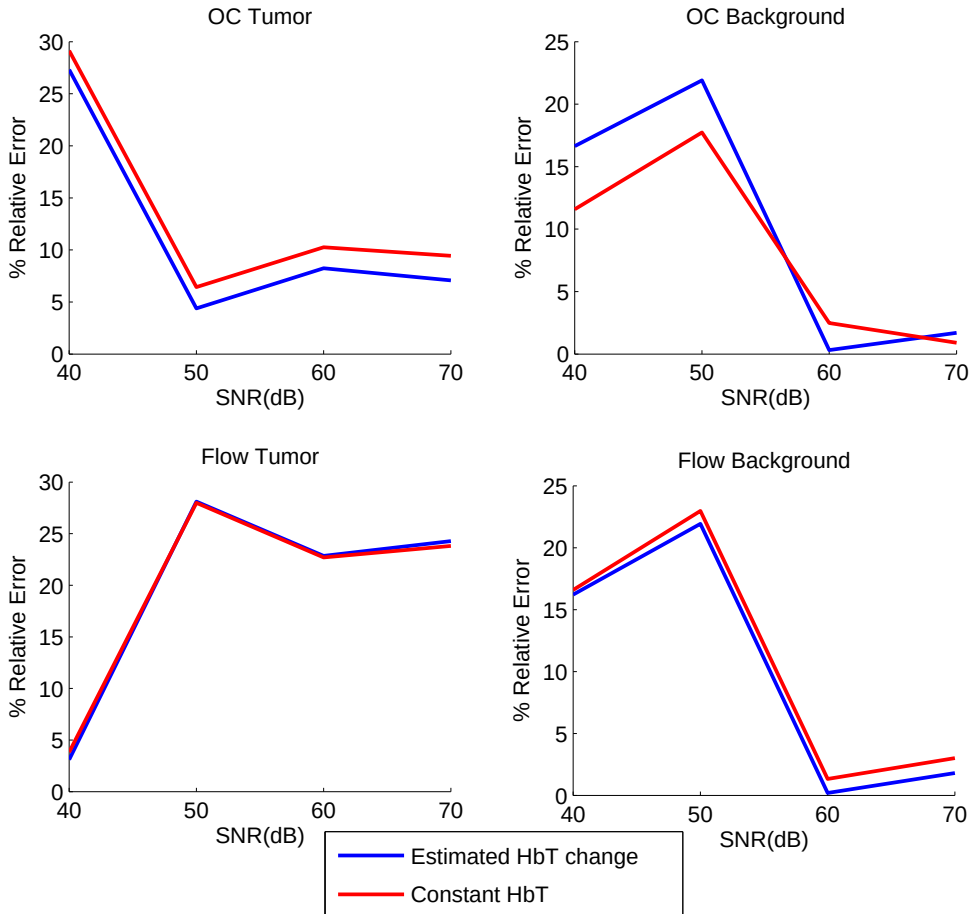

Figure 3.4 Relative error for fits using estimated HbT_t rate of change and constant HbT_t.

Another analysis we did is to see if our new model improves the OC and F reconstructions. We used the reconstructed $[HbO_2]$ and $[HbR]$ parameters from the simulation for 90s of data, 5% rate of change per minute in $[HbT]_t$, and 60dB of SNR we Figure 3.4. Then, in order to get the OC and F reconstructions, we fitted the data to our new model, Equation 2.8, and to the old model, described by Ntuba et al [24], where $[HbT]_t$ was assumed constant. Figure 3.4 shows the comparison between the two methods. We note that on average we see very little difference in the results when we assume $[HbT]_t$ constant when it is in fact variable. The 40 dB data does not provide reliable results, thus the apparent low error in the background OC case is most likely an artifact. Thus it appears that taking into account the change in $[HbT]_t$ in our model did not give us significant improvement in our OC and F reconstructions.

3.2 One Sphere - Gradual Boundary

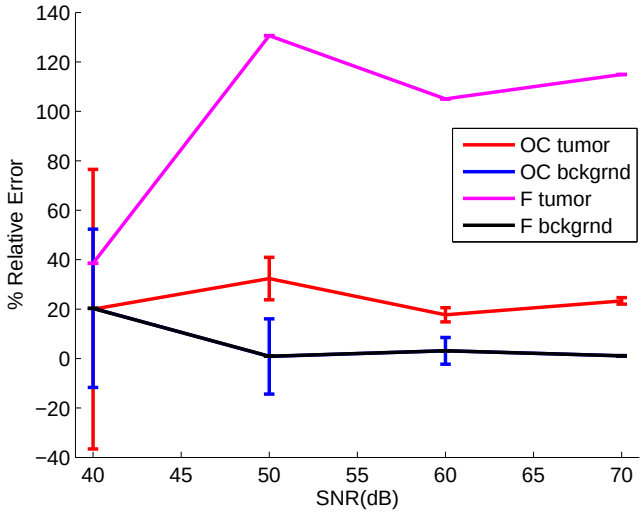

Figure 3.5 Gradual Sphere Results - 5% $[HbT]_t$ rate of change, Varying SNR(dB)

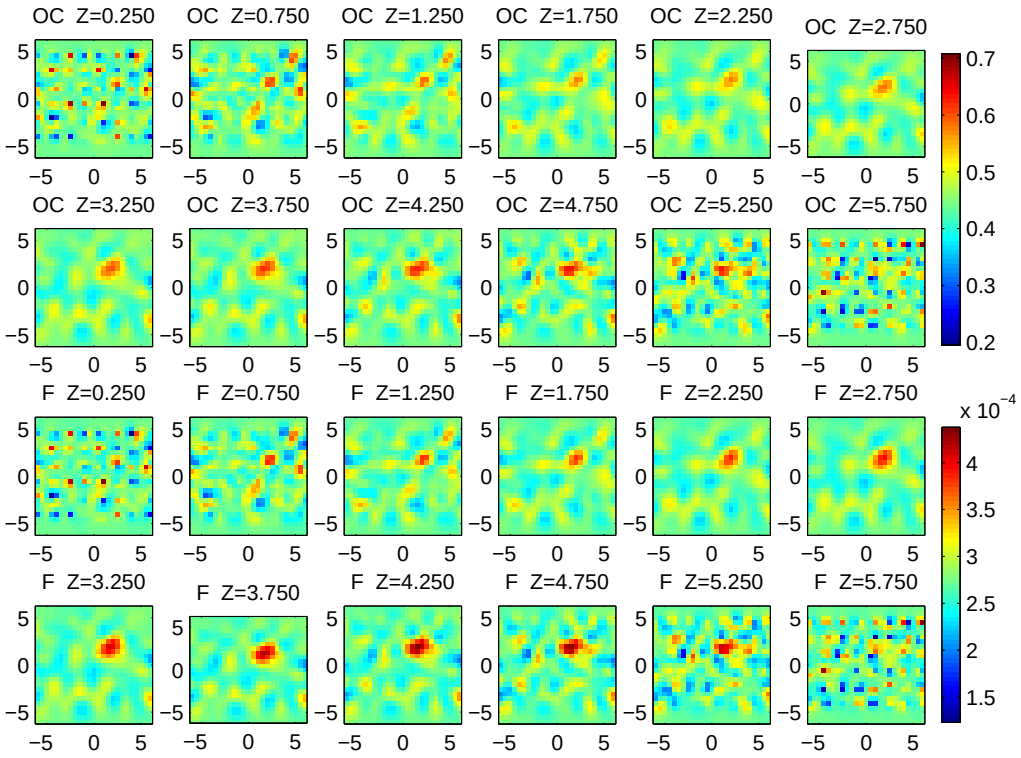

Figure 3.6 Gradual Sphere Tumor/Background Cntrast - 5% $[HbT]_t$ rate of change, 60dB SNR

Figure 3.5 shows the results of the simulations we carried out using the gradual boundary geometry. In this scenario we achieved under 20% relative error for the background OC and F, less than 40% relative error for tumor OC and very large error in the tumor F compared to the actual value we used. Even though we saw very high numerical error in our F reconstruction, we still obtained contrast between the tumor and the background, Figure 3.6, as long as the SNR was grater than 50dB.

3.3 Sphere within a Sphere (SIS)

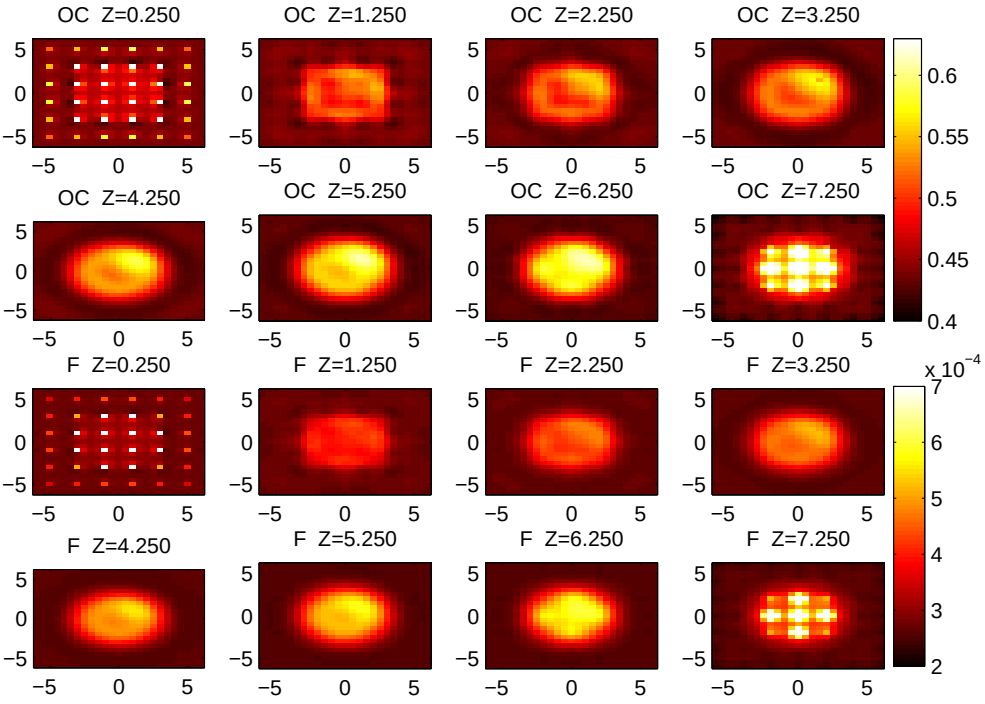

Figure 3.7 OC and F reconstructions for Geometry 3

For the third geometry we used, Fig. 2.7, we see that we obtained enough contrast to differentiate the three regions as seen in Figure 3.7. For this case we ran

one simulation with no added noise and only one rate of change in $[HbT]_t$ as a feasibility study. Even thought the initial results we obtained for this geometry were encouraging, more trials are need for more conclusive results.

3.4 Error Surfaces

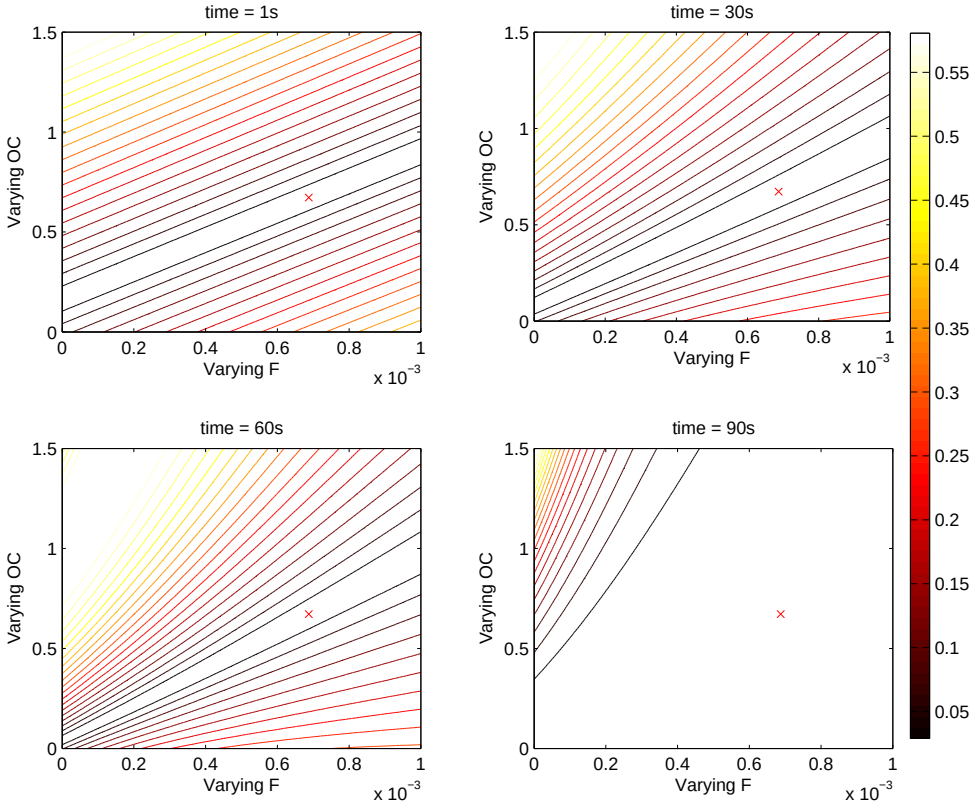

Figure 3.8 Error countours for 1s, 30s, 60s and 90s time instances

One of the observations we made in our simulation study is that the reconstructions of the tumor F returned larger errors compared to the other reconstructed parameters. In order understand this result we looked at the error surfaces when varying OC and F. Figure 3.8 depicts the error surfaces associated with equation

3.1, for the 1s, 30s, 60s and 90s time samples. For the parameters in $SO_{2,tumor}$ we used the tumor values listed in Table **??** and for $SO_2(t, F, OC)$ we varied OC from 0μM/L/s to 1.5μM/L/s and F from 0L/L/s to 0.001L/L/s. The red cross on each of the subfigures shows the location of the true value we used for the tumor OC and F.

$$E(t, F, OC) = \frac{1}{2}\|SO_{2,tumor}(t) - SO_2(t, F, OC)\|_2^2 \tag{3.1}$$

Considering the shape of the error surfaces we can see that there is more than one set of OC and F values that give minimum error. We think that F is more sensitive because the order of magnitude of the acctual parameter is lower compared to OC. In addition to that in equation 2.8 we can see that OC is only in one place in the equation, while F is in more places. Not only that but F is in the exponent and in the denominator. This could be another reason why we get greater error in the tumor F reconstructions.

Chapter 4

Conclusion

In this work we expanded the hemodynamic model described by Carp et. al. [5]. We also explored through simulations the new model, and if it gave us better results for reconstructing OC and F. The experiments we conducted included simulating three different geometries and varying different parameters, like $[HbT]_t$ rate of change, time interval, regularization parameter and SNR. Our simulation study has shown that with 1.5x OC and 2.5x F contrast we can reconstruct metabolic parameters for a spherical inclusion for reasonable experimental parameters, and that taking into account the rate of change of $[HbT]_t$ did not improve our results significantly. Further more we have noticed that by introducing a dynamic model we are able to compensate for the errors in the reconstructed tumor OC. We have also shown that we can get good reconstructions for the gradual boundary geometry and distinguish between tumor and background as long as we have SNR of higher than 50dB, which is currently what the instrument constructed at the PMI laboratory is capable of. We have also seen that we can recover contrast in an initial simulation for the sphere within sphere geometry.

Future work may include more realistic breast geometries, in order to be ready

for real data that we are expecting from instrumentation which is currently under construction at MGH. It would be interesting to see the model used when trying to reconstruct OC and F from real clinical data. Also the method described in [24] could be developed and tested to incorporate equation 2.8 into the inverse problem and directly reconstruct values for OC and F. Further exploring why the tumor F is more sensitive and why the relative error in its reconstruction is larger may also be of interest. To improve the results of the fit a better way of estimating a and b in Equation 2.2 could be used.

Bibliography

[1] R. L. Barbour, H. L. Graber, Y. Pei, S. Zhong, and C. H. Schmitz. Optical tomographic imaging of dynamic features of dense-scattering media. *J. Opt. Soc. Am. A.*, 18(12):3018–3036, 2001.

[2] R. Beaney, A. Lammertsma, T. Jones, C. Mckenzie, and K. Halnan. Positron emission tomography for in-vivo measurement of regional blood flow, oxygen utilisation, and blood voluem in patients with breast carcinoma. *The Lancet*, 1(8369):131–134, 1984.

[3] D. A. Boas, D. H. Brooks, E. L. Miller, C. A. DiMarzio, M. Kilmer, R. J. Gaudette, and Q. Zhang. Imaging the body with diffuse optical tomography. *IEEE Signal Processing Magazine*, 18(6):57–75, 2001.

[4] Bozkurt and Onaral. Safety assessment of near infrared light emitting diodes for diffuse optical measurements. *BioMedical Engineering OnLine*, 3(9):57–75, 2004.

[5] S. A. Carp, T. Kauffman, Q. Fang, E. Rafferty, R. Moore, D. Kopans, and D. Boas. Compression-induced changes in the physiological state of the breast as observed through frequency domain photon migration measurements. *Journal of Biomedical Optics*, 11(6), 2006.

[6] A. Cerussi, N. Shah, D. Hsiang, A. Durkin, J. Butler, and B.J. Tromberg. In vivo absorption, scattering, and physiologic properties of 58 malignant breast tumors determined by broadband diffuse optical spectroscopy. *J. Biomed. Opt.*, 11(4), 2006.

[7] W. F. Chheng, A. J. Prahl, and A. J. Welch. A review of the optical properties of biological tissues. *IEEE J. Quantum Electron.*, 26:2166–2185, 1990.

[8] R. Choe, A. Corlu, K. Lee, T. Durduran, S. D. Konecky, M. Grosicka-Koptyra, S. R. Arridge, B. J. Czerniecki, D. L. Fraker, A. DeMichele, B. Chance, M. A. Rosen, and A. G. Yodh. Diffuse optical tomography of breast cancer during neoadjuvant chemotherapy: A case study with comparison to mri. *Medical Physics*, 32(4), 2005.

[9] T.F. Coleman and Y. Li. On the convergence of reflective newton methods for large-scale nonlinear minimization subject to bounds. *Mathematical Programming*, 67(2):189–224, 1994.

[10] T.F. Coleman and Y. Li. An interior, trust region approach for nonlinear minimization subject to bounds. *SIAM Journal on Optimization*, 6:418–445, 1996.

[11] J. Delille, P. J. Slanetz, E. D. Yeh, D. B. Kopans, and L. Garrido. Breast cancer: Regional blood flow and blood volume measured with magnetic susceptibility-based mr imaging - initial results. *Radiology*, 223:558–565, 2003.

[12] T. Durduran, R. Choe, G. Yu, C. Zhou, J. C. Tchou, B. Czerniecki, and A. G. Yodh. Diffuse optical measurements of blood flow in breast tumors. *Optics Letters*, 30(21), 2005.

[13] J. B. Fishkin and E. Gratton. Propagation of photon-density waves in strongly scattering media containing an absorbing semi-infinite plane bounded by a straight edge. *J. Opt. Soc. Am. A.*, 10(1), 1993.

[14] J. Folkman. The influence of angiogenesis research on management of patients with breast cancer. *Breast Cancer Res. Treat.*, 36:109–118, 1995.

[15] G. Gulsen, O. Birgul, M. B. Unlu, R. Shafiiha, and O. Nalcioglu. Combined diffuse optical tomography (dot) and mri system for cancer imaging in small animals. *Technology in Cancer Research and Treatment*, 5(4):351–363, 2006.

[16] J. C. Hebden, H. Veenstra, H. Dehghani, E. M. C. Hillman, M. Schweigner, S. R. Arridge, and D. T. Delpy. Three-dimensional time-resolved optical tomography of a conical breast phantom. *Applied Optics*, 40(19):3278–3287, 2001.

[17] E. Heffer, V. Pera, O. Schutz, H. Siebold, and S. Fantini. Near-infrared imaging of the human breast: complementing hemoglobin concentration maps with oxygenation images. *J. Biomed. Opt.*, 9(6):1152–1160, 2004.

[18] D. K. Joseph, T. J. Huppert, M. A. Franceschini, and D. A. Boas. Diffuse optical tomography system to image brain activation with improved spatial resolution and validation with functional magnetic resonance imaging. *Applied Optics*, 45(31), 2006.

[19] J. C. Lagarias, J. A. Reeds, M. H. Wright, and P. E. Wright. Convergence properties of the nelder-mead simplex method in low dimensions. *SIAM Journal of Optimization*, 9(1):112–147, 1998.

[20] A. Li, G. Boverman, Y. Zhang, D. Brooks, E. L. Miller, M. Kilmer, Q. Zhang, E. M. C. Hillman, and D. A. Boas. Optimal linear inverse solution with multiple priors in diffuse optical tomography. *Applied Optics*, 44(10), 2005.

[21] A. Li, Q. Zhang, J. P. Culver, E. L. Miller, and D. A. Boas. Reconstructing chromosphere concentration images directly by continuous-wave diffuse optical tomography. *Optics Letters*, 29(3), 2004.

[22] T. O. McBride, B. W. Pogue, S. Poplack, S. Soho, W. A. Wells, S. Jiang, U. L. Osterberg, and K. D. Paulsen. Multispectral near-infrared tomography: a case study in compensating for water and lipid content in hemoglobin imaging of the breast. *J. Biomed. Opt.*, 7(1):72–79, 2002.

[23] S. Nioka and B. Chance. Nir spectroscopic detection of breast cancer. *Technology in Cancer Research and Treatment*, 4(5), 2005.

[24] D. T. Ntuba. Reconstructing hemodynamic parameters in diffuse optical tomographic breast imaging. Master's thesis, Northeastern University, Boston, MA, 2006.

[25] M. A. O'Leary, D. A. Boas, B. Chance, and A. G. Yodh. Experimental images of heterogeneous turbid media by frequency-domain diffusing-photon tomography. *Optics Letters*, 20(5):426–428, 1995.

[26] B. W. Pogue, S. P. Poplack, T. O. McBride, W. A. Wells, K. A. Osterman, U. L. Osterberg, and K. D. Paulsen. Quantitative hemoglobin tomogrpahy with diffuese near-infrared spectroscopy: pilot results in the breast. *Radiology*, 218:261–266, 2001.

[27] A. Rice and C. M. Quinn. Angiogenesis, thrombospodin, and ductal carcinoma in situ of the breast. *Journal Clinical Pathology*, 55:569–574, 2002.

[28] C. H. Schmitz, D. P. Klemer, R. Hardin, M. S. Katz, P. Yaling, H. L. Graber, M. B. Levin, R. D. Levina, N. A. Franco, W. B. Solomon, and R. L. Barbour.

Design and implementation of dynamic near-infrared optical tomographic imaging instrumentation for simultaneous dual-breast measurements. *Applied Optics*, 44(11):2140–2153, 2005.

[29] C. B. J. H. Wilson, A. A. Lammertsma, C. G. McKenzie, K. Sikora, and T. Jones. Measurements of blood flow and exchanging water space in breast tumors using positron emission tomography: A rapid and noninvasive dynamic method. *Cancer Research*, 152:1592–1597, 1992.

[30] Q. Zhang, T. J. Brukilacchio, A. Li, J. J. Stott, T. Chaves, E. Hillman, T. Wu, M. Chorlton, E. Rafferty, R. Moore, D. Kopans, and D. Boas. Coregistered tomographic x-ray and optical breast imaging: initial results. *Journal of Biomedical Optics*, 10(2), 2005.

Appendix A

Hemodynamic Model

Solution for the Mass Balance Equation with $[HbT]_{tissue}$ changing linearly

Assumptions: Linear change in total hemoglobin:

$$[HbT]_t(t) = a + bt \tag{A.1}$$

$$F_{out} = F_{in} - \frac{V_t}{[HbT]_{bl}} \frac{d[HbT]_t(t)}{dt} = F_{in} - \frac{V_t b}{[HbT]_{bl}}$$

$$\frac{F_{out}}{V_t} = \frac{F_{in}}{V_t} - \frac{b}{[HbT]_{bl}} \tag{A.2}$$

Then the mass balance equation becomes:

$$\frac{d[HbO]}{dt} = -\frac{OC}{4V_t} + \frac{F_{in}}{V_t}[HbT]_{bl} SvO_2$$

If $SO_2(t) = \frac{[HbO]}{[HbT]_t}$, then $\frac{d[HbO]}{dt} = \frac{d[HbT]_t}{dt} SO_2 + \frac{dSO_2}{dt}[HbT]_t$

$$\frac{dSO_2}{dt} = \frac{1}{[HbT]_t}\left(\frac{d[HbO]}{dt} - \frac{d[HbT]_t}{dt} SO_2\right)$$

$$\frac{dSO_2}{dt} = \frac{1}{[HbT]_t}\left(-bSO_2 - \frac{OC}{4V_t}[HbT]_t - \frac{F_{in}}{V_t}SaO_2 - \frac{F_{out}}{V_t}[HbT]_{bl}SvO_2\right)$$

$$SvO_2 = 2SO_2 - SaO_2 \tag{A.3}$$

$$\frac{dSO_2}{dt} = \frac{1}{a+bt}\left(-bSO_2 - \frac{OC}{4V_t} + \frac{F_{in}}{V_t}[HbT]_{bl}SaO_2 - \frac{F_{out}}{V_t}[HbT]_{bl}\left(2SO_2 - SaO_2\right)\right) \tag{A.4}$$

Combining equations A.4 and A.2 we get,

$$\frac{dSO_2}{dt} = \frac{1}{a+bt}\Bigg(- bSO_2 - \frac{OC}{4V_t} + \frac{F_{in}}{V_t}[HbT]_{bl}SaO_2 - \left(\frac{F_{in}}{V_t} - \frac{b}{[HbT]_{bl}}\right)[HbT]_{bl}\left(2SO_2 - SaO_2\right)\Bigg) \tag{A.5}$$

$$\frac{dSO_2}{dt} = \frac{1}{a+bt}\Bigg(- bSO_2 - \frac{OC}{4V_t} + \frac{F_{in}}{V_t}[HbT]_{bl}SaO_2 - 2\left(\frac{F_{in}}{V_t} - \frac{b}{[HbT]_{bl}}\right)[HbT]_{bl}SO_2 - \left(\frac{b}{[HbT]_{bl}}\right)[HbT]_{bl}SaO_2\Bigg) \tag{A.6}$$

$$\frac{dSO_2}{dt} = \frac{1}{a+bt}\left(-\frac{OC}{4V_t} + 2\frac{F_{in}}{V_t}[HbT]_{bl}SaO_2 - 2\frac{F_{in}}{V_t}[HbT]_{bl}SO_2 + bSO_2 - bSaO_2\right)$$

$$\frac{dSO_2}{dt} = \frac{1}{a+bt}\left(SO_2\left(b - 2\frac{F_{in}}{V_t}[HbT]_{bl}\right) - SaO_2\left(b - 2\frac{F_{in}}{V_t}[HbT]_{bl}\right)\right) \tag{A.7}$$

For simplicity we introduce some notation.

$$x = SO_2(t)$$

$$x(0) = SO_{2,init}$$

$$c = b - 2\frac{F_{in}}{V_t}[HbT]_{bl}$$

$$d = -SaO_2\left(b - 2\frac{F_{in}}{V_t}[HbT]_{bl}\right) - \frac{OC}{4V_t}$$

Then equation A.7 becomes:

$$\frac{dx}{dt} = \frac{xc+d}{a+bt}$$

$$\frac{dt}{a+bt} = \frac{dx}{xc+d}$$

$$\frac{ln\,(a+bt)}{b} = \frac{ln\,(xc+d)}{c} + A$$

Where A is the indegration constant.

$$\frac{c}{b}ln\,(a+bt) = ln\,(xc+d) + Ac$$

$$ln\,(a+bt)^{\frac{c}{b}} = ln\,(xc+d) + Ac$$

$$ln\,(xc+d) - ln\,(a+bt)^{\frac{c}{b}} = -Ac$$

$$ln\left(\frac{xc+d}{(a+bt)^{\frac{c}{b}}}\right) = -Ac$$

$$\frac{xc+d}{(a+bt)^{\frac{c}{b}}} = e^{-Ac}$$

$$xc + d = e^{-Ac}\,(a+bt)^{\frac{c}{b}}$$

$$x = \frac{e^{-Ac}\,(a+bt)^{\frac{c}{b}} - d}{c} \tag{A.8}$$

Next we solve for the integration constant A by using the initial condition below:

$$SO_{2,init} = x(0) = \frac{e^{-Ac}a^{\frac{c}{b}} - d}{c}$$

$$e^{-Ac} = \frac{cSO_{2,init} + d}{a^{\frac{c}{b}}}$$
$$-Ac = \ln\left(\frac{cSO_{2,init} + d}{a^{\frac{c}{b}}}\right)$$

$$A = \ln\left(\frac{cSO_{2,init} + d}{a^{\frac{c}{b}}}\right)^{\frac{1}{-c}} \tag{A.9}$$

Substituting A back to equation A.8 we get,

$$x = \frac{e^{-c\ln\left(\frac{cSO_{2,init}+d}{a^{\frac{c}{b}}}\right)^{\frac{1}{-c}}}(a+bt)^{\frac{c}{b}} - d}{c}$$

$$x = \frac{\left(\frac{cSO_{2,init}+d}{a^{\frac{c}{b}}}\right)(a+bt)^{\frac{c}{b}} - d}{c}$$

$$x = \frac{1}{c}\left((cSO_{2,init} + d)\left(\frac{a+bt}{a}\right)^{\frac{c}{b}} - d\right)$$

Substituting the constants back in, we get:

$$x = \frac{1}{b - 2\frac{F_{in}}{V}[HbT]_{bl}}\Bigg(\Big(\Big(b - 2\frac{F_{in}}{V}[HbT]_{bl}\Big)SO_{2,init} + \big(-SaO_2\big(b - 2\frac{F_{in}}{V}[HbT]_{bl}\big) - \frac{OC}{4V}\big)\Big)$$
$$\left(\frac{a+bt}{a}\right)^{\frac{b-2\frac{F_{in}}{V}[HbT]_{bl}}{b}} - \left(-SaO_2\left(b - 2\frac{F_{in}}{V}[HbT]_{bl}\right) - \frac{OC}{4V}\right)\Bigg) \tag{A.10}$$

$$SO_2(t) = \frac{1}{b - 2\frac{F_{in}}{V}[HbT]_{bl}}\Bigg(\left((SO_{2,init} - SaO_2)\left(b - 2\frac{F_{in}}{V}[HbT]_{bl}\right) - \frac{OC}{4V}\right)\left(\frac{a+bt}{a}\right)^{\frac{b-2\frac{F_{in}}{V}[HbT]_{bl}}{b}}$$
$$+ SaO_2\left(b - 2\frac{F_{in}}{V}[HbT]_{bl}\right) + \frac{OC}{4V}\Bigg) \tag{A.11}$$

$$SO_2(t) = \Bigg(\left((SO_{2,init} - SaO_2) - \frac{OC}{4V\left(b - 2\frac{F_{in}}{V}[HbT]_{bl}\right)}\right)\left(\frac{a+bt}{a}\right)^{\frac{b-2\frac{F_{in}}{V}[HbT]_{bl}}{b}}$$
$$+ SaO_2 + \frac{OC}{4V\left(b - 2\frac{F_{in}}{V}[HbT]_{bl}\right)}\Bigg) \tag{A.12}$$

$$SO_2(t) = SO_{2,init}\left(\frac{a+bt}{a}\right)^{\frac{b-2\frac{F_{in}}{V}[HbT]_{bl}}{b}} + SaO_2\left(1-\left(\frac{a+bt}{a}\right)^{\frac{b-2\frac{F_{in}}{V}[HbT]_{bl}}{b}}\right) + \frac{OC}{4V\left(b-2\frac{F_{in}}{V}[HbT]_{bl}\right)}\left(1-\left(\frac{a+bt}{a}\right)^{\frac{b-2\frac{F_{in}}{V}[HbT]_{bl}}{b}}\right) \tag{A.13}$$

$$SO_2(t) = SO_{2,init}\left(\frac{a+bt}{a}\right)^{1-2\frac{F_{in}}{V}\frac{[HbT]_{bl}}{b}} + \left(SaO_2 + \frac{OC}{4V\left(b-2\frac{F_{in}}{V}[HbT]_{bl}\right)}\right)\left(1-\left(\frac{a+bt}{a}\right)^{1-2\frac{F_{in}}{V}\frac{[HbT]_{bl}}{b}}\right) \tag{A.14}$$